Inhibition of cAMP-Dependent Protein Kinase under Conditions Occurring in the Cardiac Dyad during a Ca²⁺ Transient

Peter P. Jones,*[†] Hojjat Bazzazi,[†‡] Gary J. Kargacin,[†] and John Colyer*

*Institute of Membrane and Systems Biology, University of Leeds, Leeds LS2 9JT, United Kingdom; [†]Department of Physiology and Biophysics, University of Calgary, Calgary, Alberta T2N 4N1, Canada; and [‡]Department of Biomedical Engineering, The Johns Hopkins University, Baltimore, Maryland 21205

ABSTRACT   The space between the t-tubule invagination and the sarcoplasmic reticulum (SR) membrane, the dyad, in ventricular myocytes has been predicted to experience very high $[Ca^{2+}]$ for short periods of time during a Ca^{2+} transient. The dyadic space accommodates many protein kinases responsible for the regulation of Ca^{2+} handling proteins of the cell. We show in vitro that cAMP-dependent protein kinase (PKA) is inhibited by high $[Ca^{2+}]$ through a shift in the ratio of CaATP/MgATP toward CaATP. We further generate a three-dimensional mathematical model of Ca^{2+} and ATP diffusion within dyad. We use this model to predict the extent to which PKA would be inhibited by an increased CaATP/MgATP ratio during a Ca^{2+} transient in the dyad in vivo. Our results suggest that under normal physiological conditions a myocyte paced at 1 Hz would experience up to 55% inhibition of PKA within the cardiac dyad, with inhibition averaging 5% throughout the transient, an effect which becomes more pronounced as the myocyte contractile frequency increases (at 7 Hz, PKA inhibition averages 28% across the dyad throughout the duration of a Ca^{2+} transient).

INTRODUCTION

The calcium concentration ($[Ca^{2+}]$) in cardiac myocytes varies significantly both spatially and temporally during a contraction. Cytosolic-free calcium ($[Ca^{2+}]_{free}$) typically averages ~150 nM at rest but increases to ~1 μM during a contraction, with half-maximal contraction occurring at ~600 nM (1). Subsequent relaxation occurs when $[Ca^{2+}]_{free}$ falls to ~200 nM (2). In organelles within the myocyte such as the sarcoplasmic reticulum (SR), the $[Ca^{2+}]$ is much more difficult to measure accurately. Shannon and Bers (3) have estimated the total SR $[Ca^{2+}]$ in quiescent myocytes to be as high as 14 mM although the free $[Ca^{2+}]$ in the SR lumen is likely to be lower than this.

During contraction, Ca^{2+} enters the myocyte through the voltage-gated L-type calcium channels (dihydropyridine receptors, DHPR) in the t-tubular invagination of the sarcolemma. This triggers an additional, greater release of Ca^{2+} from the SR through the ryanodine receptors (RYR), a process termed calcium-induced calcium release (CICR, (4)). The cell architecture is such that both Ca^{2+} entry into the cell and Ca^{2+} release from the SR deposit Ca^{2+} into the cardiac dyad, the physical space formed between the t-tubule and the opposing SR membrane. The dyadic cleft between the t-tubule and SR membrane is typically a gap of ~10 nm and covers an area with a radius of 200 nm (5). These dimensions are sufficiently small to result in restricted diffusion of soluble components, the diffusion of which is further restricted by the protrusion of protein domains, particularly RYR do-

mains, into the dyadic space. The movement of Ca^{2+} in this space has not been observed experimentally, as the kinetics of movement and the small size of the dyad impose technical barriers that are difficult to overcome. Instead, a number of groups has used computational methods to predict dyadic free calcium $[Ca^{2+}]_{dyad}$, which range from ~10 μM to ~7 mM (5–9).

Many proteins resident in the dyadic region are controlled by both Ca^{2+} and site-specific phosphorylation (10). It has been long established that phosphorylation of DHPR increases Ca^{2+} current (I_{Ca}), probably by increasing the open probability (P_o) of the channel (11). Ca^{2+} also regulates RYR. Submicromolar Ca^{2+} is capable of activating RYR, but the maximal P_o is reached at ~100 μM, with higher (>5 mM) Ca^{2+} leading to inactivation of the channel (12,13). Although it is well established that both cAMP-dependent protein kinase (PKA) and calcium-calmodulin-dependent kinase II (CaMKII) phosphorylate RYR (14–16), the role of phosphorylation of RYR remains a contentious issue. It has been shown that RYR can be phosphorylated by both PKA and CaMKII in vitro at Ser-2809 (or Ser-2808, in humans) (14,15,17). Changes occurring upon in vitro phosphorylation at Ser-2809 are significant, including an increased P_o (15,17), the abrogation of the inhibitory effects of calmodulin (CaM) (15) and Mg^{2+} (18), an increased Ca^{2+} sensitivity of P_o (19), dissociation of regulatory factors (e.g., FKBP12.6), expression of subconductance states, and the expression of channel activity at diastolic $[Ca^{2+}]_{free}$ (17). Clinically, hyperphosphorylation of RYR at Ser-2808 has been described in situations such as heart failure, suggesting abnormal control of the phosphorylation status may contribute to abnormal Ca^{2+} handling (20), although more recent studies in vivo have noted no increase in Ser-2808

phosphorylation in failing canine, rat, or human hearts (21). Ser-2030 has also been described as a target for PKA phosphorylation, with a recent study suggesting that it is the major RYR phosphorylation target in response to β-adrenergic stimulation (21). To date no effect on Ca^{2+} handling has been reported relating to RYR Ser-2030 phosphorylation.

The RYR channels may play a more important role in β-adrenergic signaling as scaffold proteins, as they form a complex that localizes PKA and phosphatases 1 and 2A in the dyad (17). This is thought to ensure efficient local control of the phosphorylation status of RYR and other neighboring proteins.

A number of protein kinases have been reported to be affected by high $[Ca^{2+}]$ because of the effect of Ca^{2+} on the level of MgATP. An increase in $[Ca^{2+}]$ shifts the MgATP $\Leftrightarrow$ CaATP equilibrium toward CaATP, thus reducing MgATP. Additionally, specific ATP hydrolyzing proteins such as Juvenile Hormone Diol kinase (22) and the H^+,K^+-ATPase (23) will bind CaATP but not hydrolyze it efficiently. In these enzymes CaATP blocks the access of MgATP to the catalytic sites of the kinases and so is effectively a competitive inhibitor. Bhatnagar et al. (24) have reported that PKA will bind CaATP with a similar apparent affinity as MgATP but cannot hydrolyze CaATP to CaADP. These data suggest that PKA will be competitively inhibited by Ca^{2+} (through an increase in CaATP). If this occurs, it poses an interesting situation for the control of dyadic proteins by phosphorylation, where the normal extremes of $[Ca^{2+}]_{dyad}$ may affect kinase activity.

Here we show that PKA activity is inhibited by high $[Ca^{2+}]$ as a result of an increase in [CaATP]. We have also developed a computer model of a ventricular myocyte incorporating the dyad that allows us to predict the extent to which PKA inhibition would occur in vivo.

METHODS

Materials

PKA was purchased from Upstate (Charlottesville, VA), PL919Y (synthetic peptide substrate, RSAIRRASTIEY-amide) was synthesized by Neosystem (Strasbourg, France), [γ-^{32}P]ATP was obtained from MP Biomedicals (Irvine, CA), and P81 paper was purchased from Whatman (Brentford, UK). All other chemicals were purchased from Sigma-Aldrich (Poole, UK).

Phosphorylation assays

Phosphorylation reactions were conducted at 37°C in 100 μl buffer containing 400 U (1 U is 1 pmol phosphate incorporation into PL919Y at 37°C per min) PKA, 0.1 mM PL919Y, and 50 mM histidine (pH 7.0), 5 or 25 mM MgSO$_4$, 6.25 mM NaF, 1 mM EGTA, and CaCl$_2$ to achieve $[Ca^{2+}]_{free}$ of 3 μM–10 mM (calculated using Bound and Determined (BAD) 4.42 (25)). After 2 min of equilibration the phosphorylation reaction was initiated by the addition of 0.1 mM [γ-^{32}P]ATP (0.1 μCi/nmol, final concentration to 10 μM). After 1 min of incubation the reaction was terminated by the addition of 100 μl 1% (v/v) H$_3$PO$_4$ to the sample and transferring 180 μl of sample to P81 paper. P81 paper was then washed 4 × 5 min in 1% (v/v) H$_3$PO$_4$ before drying. Incorporated [γ-^{32}P] was determined by scintillation counting in Emulsifier-safe using a Packard TriCarb 1900TR scintillation counter, counting for 2 min per sample (both from Canberra-Packard Ltd., Pangbourne, UK).

Three-dimensional model of a sarcomere

The three-dimensional model of the half cardiac sarcomere is shown diagrammatically in Fig. 1. The sarcomere was cylindrical in shape (radius 500 nm; length 1000 nm). Ca^{2+} diffusion and regulatory processes were described by the following partial differential equation, which was solved using the implicit Euler's method of solution

$$\frac{\partial [Ca]}{\partial t} = \frac{D}{r}\left\{\frac{\partial}{\partial r}\left(r\frac{\partial [Ca]}{\partial r}\right) + \frac{\partial}{\partial \theta}\left(\frac{1}{r}\frac{\partial [Ca]}{\partial \theta}\right) + \frac{\partial}{\partial z}\left(r\frac{\partial [Ca]}{\partial z}\right)\right\} + F(r,\theta,z,[Ca],t), \tag{1}$$

where r, θ, and z are the radial, angular, and length dimensions in a cylindrical coordinate system, D is the diffusion coefficient, and $F(r,\theta,z,[Ca],t)$ is a function describing the position, concentration, and time-dependent Ca^{2+} regulatory processes and buffering included in the model. Similar equations were used to describe the diffusion of Mg^{2+} and the Ca^{2+} and Mg^{2+}-bound forms of ATP and ADP in the model. The modeled cell segment was divided into 50 radial elements (each one extending 10 nm in the radial direction), 50 length elements (10-nm long within the dyad, 20.6-nm long outside of the dyad), and 20 (18°) angular elements. The SR was represented by a disk located 10 nm from the plasma membrane with a radius of 200 nm, and a thickness of 20 nm in the z-direction (see Fig. 1). These dimensions are in keeping with those reported in the literature (5). At the start of the simulations, extracellular $[Ca^{2+}]$ was assumed to be 1 mM, SR luminal $[Ca^{2+}]$ was assumed to be 0.7 mM, and resting $[Ca^{2+}]_{free}$ was assumed to be 100 nM (26). Euler's method of solution of Eq. 1 requires that diffusion be computed into one element at each position beyond the boundaries of the model. This was achieved by setting all of the components in each element
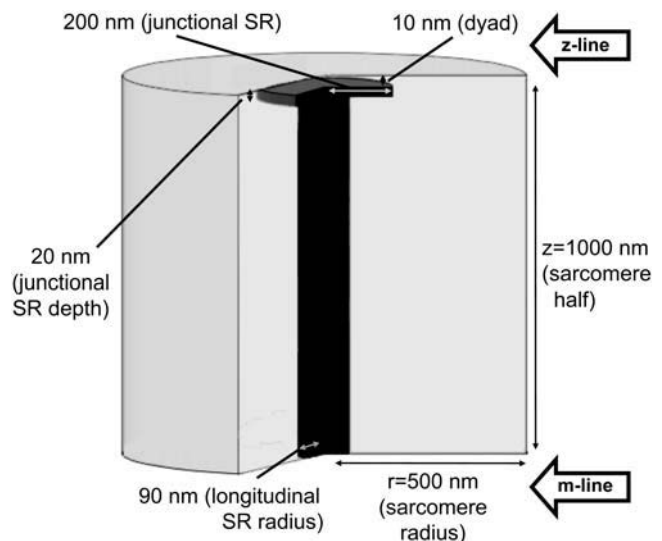

FIGURE 1 Cartoon of the computer model representing half of a sarcomere (Z-line to M-line). The position in the sarcomere is expressed in cylindrical coordinates (r,z,θ). The model is a cylinder with radius, r = 500 nm, length, z = 1000 nm. The junctional SR is modeled as an impermeable disk with radius, $r1$ = 200 nm, depth = 20 nm, situated 10 nm from the Z-line surface. Longitudinal SR is represented as a cylinder with radius = 90 nm and length = 970 nm. Free diffusion was allowed to occur throughout the longitudinal SR; however, SERCA uptake also occurred in this region. In r, the model is divided into 10-nm elements; in z the element size is 10 nm above and including the SR and 20.6 nm below, radially, the model is divided into 20 even segments. Calcium enters the model through the 20 radial segments at $r = 1$. Free $[Ca^{2+}]$, CaATP, MgATP, CaADP, and MgATP are obtained for each element at 1-ms intervals.

beyond the boundary equal to the value at the boundary as described previously (27).

Ca^{2+} influx and release into the dyadic space was modeled by increasing the [Ca^{2+}] in all the radial elements where r and $z = 1$ (i.e., the center 20 elements of the dyadic space). Ca^{2+} entry into each of the 20 elements was modeled using the following exponential equation:

$$\frac{\partial[Ca]}{\partial t} = B e^{-t/\tau_{\text{off}}} \times \left(1 - e^{-t/\tau_{\text{on}}}\right), \qquad (2)$$

where B is a current term and τ_{off} and τ_{on} are time constants of 3 and 40 ms, respectively (10), for the rising and falling phases of the Ca^{2+} transient. The current term was chosen so that the Ca^{2+} increase in the whole myocyte (20 pl volume) was 16 μM and is consistent with Ca^{2+} increases in the literature (5,28,29). An exponential increase and decay in [Ca^{2+}] was chosen over a square pulse to better represent the cooperative opening and closing of both DHPR and RYR. Ca^{2+} removal from the cytosol in the model was assumed to occur through uptake into the SR and extrusion across the plasma membrane. Uptake into the SR occurred on the cytosolic surface of the SR and throughout a cylinder (representing longitudinal SR), radius 90 nm, extending from the

dyad opposing the SR surface to the distal end of the model (Fig. 1). Uptake into the SR mediated by SERCA was described by the Hill equation,

$$\frac{\partial[Ca]}{\partial t} = A \times V_{\max} \frac{[Ca]^{\text{n}}}{K_{\text{m}}^{\text{n}} + [Ca]^{\text{n}}}, \qquad (3)$$

where A is the number pumps per element, K_{m} is the [Ca^{2+}] required for half-maximal uptake velocity, $V_{\max}$ is the theoretical maximum uptake velocity, and n is the Hill coefficient for uptake (see Table 1 for values).

Extrusion across the plasma membrane occurred at the Z-line, at all voxels outside of the dyad ($z = 1$, $r >$ dyad radius). Extrusion was also described by Eq. 3, with $n = 1$ (see Table 1 for a complete list of values).

As described previously (27), passive leak from the SR and extracellular spaces was described by equations of the form

$$\frac{\partial[Ca]}{\partial t} = K_{\text{leak}}([Ca]_{\text{x}} - [Ca]_{\text{free}}); \qquad (4)$$

where [Ca]$_{\text{x}}$ is the free Ca^{2+} within the SR or in the extracellular space (set as 0.7 and 1 mM, respectively), and leak constants (K_{leak}) were adjusted so that

TABLE 1   Values used for mathematical model

Ion or molecule	Concentration (mM)	Diffusion (μm^{2}s^{-1})
Free Ca^{2+}	0.0001*	100 dyad*, 300 cytosol*
Free Mg^{2+}	1[†]	63 dyad*[‡], 190 cytosol[‡]
Total ATP	7[†]	60 dyad*[§], 180 cytosol*[§]
Total ADP	0.005[†]	60 dyad*[§], 180 cytosol*[§]
H$^+$	0.0001	

*Peskoff and Langer (5).
[†]Michailova and McCulloch (7).
[‡]Bernengo et al. (35).
[§]Baylor and Hollingworth (30).
Metal ATP or ADP complex diffusion was assumed to be the same as free ATP or ADP.

Buffer	k_{on} (μM^{-1}s^{-1})	k_{off} (s^{-1})	Concentration (μM)
Troponin C*[†]	32.7	19.6	70
Troponin C Ca/Mg[†‡]	2.37	0.032	140
Myosin[†]	13.8	0.46	140
Calmodulin[§]	34	238	24
Sarcolemma[¶]	100	1300	42
Membrane[‖]	100	30	15
ATP Ca**	225	45,000	7000
Mg**	125	10,875	
ADP Ca**	125	193500	5
Mg**	125	84500	
PKA MgATP[‡‡]	1.8	68	
CaATP[§§]	1.8 ± 25%	68 ± 25%	

*Gao et al. (36).
[†]Robertson et al. (37).
[‡]Pan and Solaro (38).
[§]Haiech et al. (39).
[¶]Post and Langer (40).
[‖]Bers (41).
**Michailova and McCulloch (7).
and [‡‡]Lew et al. (31).
[§§]No data available; rates based on those of MgATP (see text).

Calcium removal pathway	K_{m} (μM)	$V_{\max}$ (μMs^{-1})	Hill coefficient
SR uptake*	0.3	210	2
Plasma membrane extrusion[†]	4	70	1

*Bers (10).
[†]Blaustein and Lederer (42).

under resting conditions ($[Ca^{2+}]_{free} = 100$ nM) leak from the SR was equal to SERCA uptake and leak into the cell was equal to plasma membrane extrusion.

Buffering within the model was the same at all locations and was based upon buffering components described by Bers (10) for a rabbit ventricle, with the addition of ATP and ADP, which are capable of binding Ca^{2+} or Mg^{2+} (see Table 1 for binding constants and concentrations). The action of these buffers was described by the equation

$$\frac{\partial [X]}{\partial t} = -k_{on}([X] \times [buffer]_{free}) + k_{off}([X \cdot buffer]), \quad (5)$$

where $[X]$ is Ca^{2+} or Mg^{2+}, k_{on} and k_{off} are the on and off rates for Ca^{2+} or Mg^{2+} binding to the buffer and $[X \cdot buffer]$ is the Ca^{2+} or Mg^{2+} bound form of the buffer.

The apparent metal-ATP occupancy of PKA was calculated at microsecond intervals using the above equation (with PKA acting as the buffer, see Table 1 for binding constants and concentrations). The rate constants for the binding of CaATP to PKA were assumed to be roughly the same as MgATP. To account for possible differences in the rate constants, the on and off rates for CaATP binding to PKA were varied by $\pm 25\%$ of MgATP values in simulations. This assumption was based upon evidence that the apparent affinities of the two species for PKA are similar (24).

RESULTS

Ca^{2+} (CaATP) sensitivity of PKA

The effect of $[Ca^{2+}]$ on PKA activity was examined by measuring the phosphorylation of a peptide substrate at a variety of $[Ca^{2+}]_{free}$. Fig. 2 A shows that high $[Ca^{2+}]_{free}$ inhibits PKA activity and that this inhibitory profile is influenced by the concentration of Mg^{2+}. Raising Mg^{2+} offered some protection to the enzyme from the inhibitory potential of Ca^{2+}, consistent with the notion of competition between Ca^{2+} and Mg^{2+}. As PKA does not possess an identified Ca^{2+}-binding site, we explored the possibility that

inhibition was achieved indirectly through competition of Ca^{2+} and Mg^{2+} for ATP. As $[Ca^{2+}]_{free}$ increases (as in Fig. 2 A) it will shift the equilibrium of MgATP $\Leftrightarrow$ CaATP toward CaATP, as shown in Fig. 2 B, resulting in PKA inhibition through both a reduction in MgATP concentration, and as a consequence of CaATP-binding. Others have shown that CaATP is not a substrate for the kinase (24). Fig. 2 C shows the activity of PKA from Fig. 2 A replotted against the CaATP/MgATP ratio. The data generated with both 5 mM and 25 mM Mg^{2+} are described by the same double exponential relationship, strengthening our assumption that the inhibition of PKA is caused by the increase in the CaATP/MgATP ratio.

With the determination of the relationship between $[Ca^{2+}]$ and PKA activity, we sought to investigate whether the conditions required for the inhibition of PKA occur physiologically. The vast majority of cellular locations can be discounted because the $[Ca^{2+}]_{free}$ required to sufficiently alter the CaATP/MgATP balance would never occur. The cardiac dyad, however, may be a site where this could occur. The dyadic cleft is a highly restricted space where high levels of Ca^{2+} occur transiently during excitation contraction coupling. Predicted transient $[Ca^{2+}]_{dyad}$ in this region range between 10 μM and 7 mM (5–9). $[Ca^{2+}]$ in this range could significantly alter the CaATP/MgATP ratio, resulting in the inhibition of PKA (Fig. 2).

Computer simulation of half a sarcomere (model validation)

Many models of the cardiac sarcomere have been developed (see above), all of which in some way simplify the structure
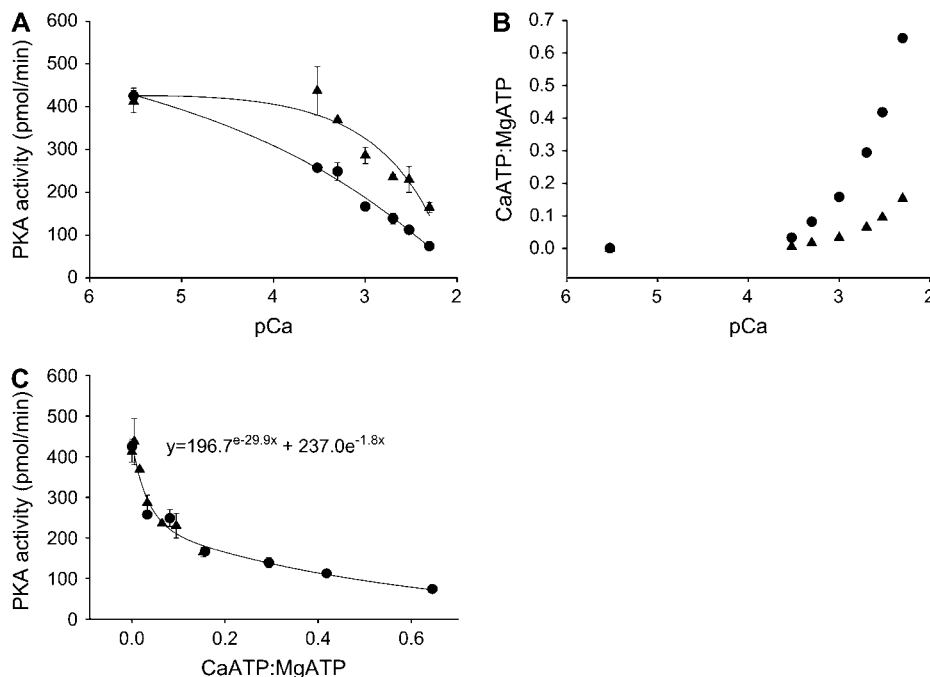

FIGURE 2 Effect of $[Ca^{2+}]_{free}$ on PKA activity. (A) PKA (400 U) was incubated at a range of $[Ca^{2+}]_{free}$ (3 μM–10 mM) for 2 min in 50 mM histidine (pH 7.0) containing 5 mM (●) or 25 mM (▲) MgSO$_4$, 6.25 mM NaF, 1 mM EGTA, and 0.1 mM PL919Y. PL919Y was phosphorylated for 1 min at 37°C after the addition of 0.1 mM ATP-γ-^{32}P (final concentration to 10 μM). The reaction was terminated by the addition of 100 μl 1% (v/v) H$_3$PO$_4$. Phosphorylated PL919Y was transferred to P81 paper, and [γ-^{32}P] incorporation was measured by scintillation counting. The background-corrected levels of incorporation are shown and represent the mean $\pm$ SE ($n = 3$). (B) Effect of increasing $[Ca^{2+}]_{free}$ on the CaATP/MgATP at total magnesium concentrations of 5 (●) and 25 mM (▲). The concentrations of CaATP and MgATP were calculated using BAD 4.42 (25). (C) Effect of CaATP/MgATP on PKA activity. Data from A were replotted using the ratio generated in B.

In panel C: $y = 196.7e^{-29.9x} + 237.0e^{-1.8x}$

to focus on a specific area of interest. In this study, we have generated a model of a half sarcomere containing a single dyadic cleft using morphological structures of realistic dimensions (SR volume, dyadic area, plasma membrane area, sarcomeric volume (5); Fig. 1) to focus on Ca^{2+} and CaATP movement and concentration in and around the dyad. The spatial elements of the model are divided into voxels using the cylindrical coordinate system (r,z,θ; see Methods), and the Ca^{2+} flux rates, Ca^{2+} diffusion rates, and Ca^{2+}-buffering characteristics are taken from the relevant literature (Table 1). The model allows for the entry of Ca^{2+} at a single site within the dyad, its free diffusion from one voxel to another, its uptake into the SR, and its efflux from the cell, thereby generating a dynamic model of Ca^{2+} homeostasis in the myocyte. To assess the predictive power of this model, and the kinetic parameters therein, we examined its ability to simulate a realistic cytosolic Ca^{2+} transient. Furthermore, we assessed the stability of the model by simulating a train of Ca^{2+} transients (9th and 10th shown in Fig. 3 A), the 10th of which is displayed in Fig. 3 B. A stable average cytosolic Ca^{2+} transient was predicted by the simulation, which rose to a peak of 680 nM at 95 ms and declined following a
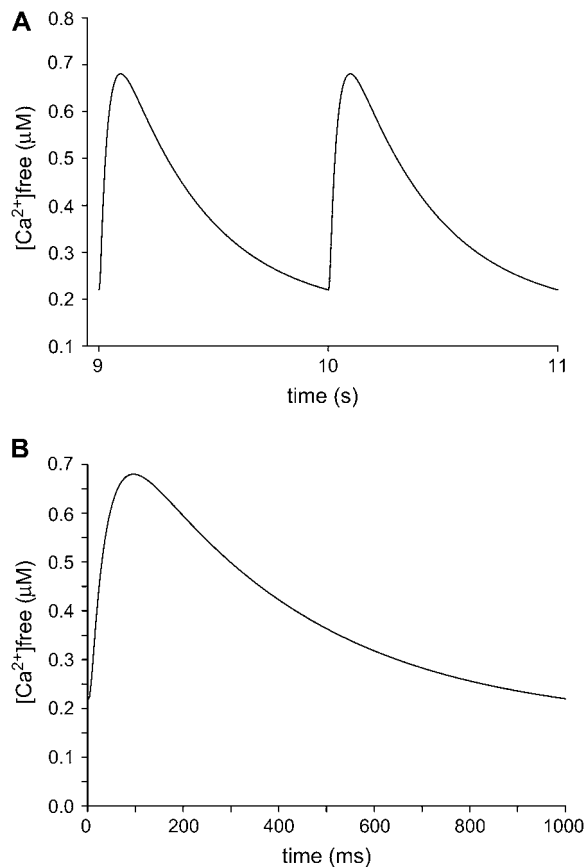

FIGURE 3 $[Ca^{2+}]_{free}$ transients generated by the mathematical model. $[Ca^{2+}]_{free}$ was averaged throughout the cytosolic elements of the model. (A) Transients 9 and 10 from a train of 20. (B) Transient generated on the 10th stimulation, expanded timescale from A.

monoexponential function ($\tau = -0.67$ s) to a diastolic $[Ca^{2+}]_{free}$ of 220 nM. These values are similar to those reported for ventricular myocytes, paced at 1 Hz (8) and by other mathematical models (7,10).

$[Ca^{2+}]_{dyad}$ during a Ca^{2+} transient

The establishment of a model that accurately simulates the average cytosolic Ca^{2+} transient allowed us to predict the $[Ca^{2+}]_{dyad}$. The $[Ca^{2+}]$ in the model was calculated at 1-ms intervals at each segment of the model (using the radial coordinate system r,z,θ). The three-dimensional plot in Fig. 4 A shows the $[Ca^{2+}]$ at $z = 1$ (the Z-line) plotted as a function of radial position and time. The shaded region represents the space within the dyadic cleft, where $[Ca^{2+}]_{dyad}$ rises to 300 μM (average concentration in the cleft; Fig. 4 C), or 2.1 mM close to the channel opening (Fig. 4 B) for a short period of time after the arrival of an action potential. These concentrations are at least 1000-fold higher than those experienced in the bulk cytosol, and these excessive concentrations are experienced almost exclusively in the dyad as a steep gradient occurs at the junction between dyad and free cytosol (Fig. 4 A). The inclusion of ATP as a diffusible Ca^{2+} buffer has dramatic effects on $[Ca^{2+}]_{dyad}$ within the cleft. Without ATP diffusion the peak $[Ca^{2+}]_{dyad}$ is almost triple that observed with ATP diffusion (data not shown). This agrees with Michailova and McCulloch (7) in illustrating the importance of ATP as a mobile Ca^{2+} buffer.

Ratio of CaATP/MgATP within the cardiac dyad during a calcium transient

In addition to predicting $[Ca^{2+}]_{free}$, our model also calculates the diffusion and concentration of ATP/CaATP/MgATP during the Ca^{2+} transient, so it is possible to calculate the CaATP/MgATP ratio generated throughout the model cell. Again the three foci of interest are the site of Ca^{2+} entry (Fig. 5 A), the dyad averaged as a whole (Fig. 5 B), and the average in the bulk cytosol (Fig. 5 C).

Although the ratio of CaATP/MgATP in the bulk cytosol undergoes a modest increase (threefold change at its maximum) as predicted by Michailova and McCulloch (7), the ratio changes greatly in the dyad throughout the calcium transient. At the point of Ca^{2+} entry the CaATP/MgATP ratio displayed a 2000-fold increase from an initial ratio of 9.4×10^{-5} to a final ratio of 0.18. This represents a change from an initial condition of 10,000 molecules of MgATP for every molecule of CaATP, to a situation where there are only six molecules of MgATP for every CaATP.

As would be expected, the CaATP/MgATP ratio observed across the whole dyad changed substantially during a single Ca^{2+} transient; however the magnitude of change was less than that observed at the channel mouth. The increase, however, is still substantial being 650-fold at its height. Using the prediction of the CaATP/MgATP generated within the
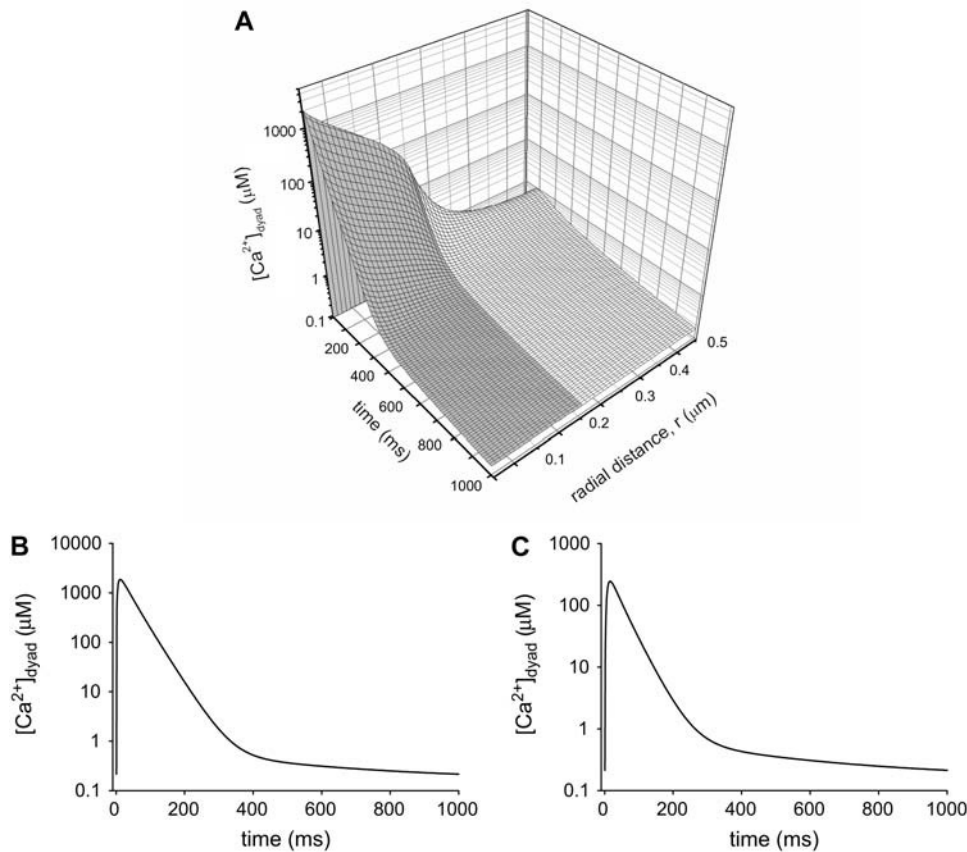
FIGURE 4 [Ca^{2+}] generated within the dyad. (*A*) Three-dimensional plots of [Ca^{2+}] at the Z-line ($z = 1$) as a function of time. The shaded region represents the dyadic space. (*B*) [Ca^{2+}] generated at $r = 1$, akin to the 10-nm space immediately surrounding the RYR and DHPR channels. (*C*) [Ca^{2+}] averaged across the whole of the dyad.

model along with the kinetic rates of CaATP and MgATP binding to PKA, we next were able to estimate the occupancy of PKA for either of the two metal ATP complexes (PKA-CaATP, PKA-MgATP, and their ratio) (see Fig. 5, *A* and *B*). We were further able to predict the impact of these changes in metal ATP occupancy on PKA activity throughout the sarcomere during a calcium transient.

The activity of PKA is reduced in the dyad of a cardiac myocyte during contraction

Having previously defined the relationship between PKA activity and the CaATP/MgATP ratio in vitro, we were able to use the CaATP/MgATP occupancy ratio of PKA to calculate the activity of PKA at each time point, relative to theoretical maximum activity of PKA, throughout the sarcomere. Fig. 6 *A* shows the activity of PKA across the t-tubule end of a sarcomere ($z = 1$, Z-line) during a Ca^{2+} transient. The shaded region illustrates the activity of PKA within the dyad. There is a gradient of PKA activity across the cleft, with maximal inhibition occurring at the point of calcium entry ($r = 1$). There is little or no effect on PKA activity beyond the radius of the cleft. At the radial edge of the cleft PKA, activity would only experience modest inhibition ($\sim$10%) due to the CaATP/MgATP at the maxima of the Ca^{2+} transient. Thus, the oscillation in PKA activity in

neighboring regions (e.g., corbular SR, longitudinal SR) would be slight. Fig. 6 *B* replots the activity of PKA at the channel mouth showing the effect of varying the kinetics of CaATP binding to PKA by ±25%. It shows there is a significant reduction in PKA activity at the channel mouth and that a 25% variation in CaATP-binding kinetics only results in ±5% shift in the relative activity of PKA. The time course of PKA inhibition within the cleft shows a maximal inhibition of 55% occurring at the point of calcium entry ($r = 1$). Fig. 6 *C* shows the average reduction in PKA activity across the whole cleft, again with inclusion of a 25% variation in CaATP-binding kinetics, here the reduction in PKA activity is 40%. In both cases the peak inhibitory effect occurs at 37 ms with maximal activity being returned around 200 ms, if one assumes a 1-Hz stimulatory frequency. Integrating the data allows us to predict the level of inhibition during both the whole and a portion of the transient. At 1 Hz this equates to an 8% reduction in PKA activity over the entire transient at the channel mouth (5% across the whole dyad). If we were to assume an increased stimulation frequency of 3 Hz (around that of exercising humans), the contraction cycle would last 333 ms, throughout which PKA activity would remain suppressed by 24% at the channel mouth (14% across the whole dyad). Increasing the frequency, yet higher, to that of small mammals (7 Hz) shows a reduction in PKA activity of nearly 47% (channel
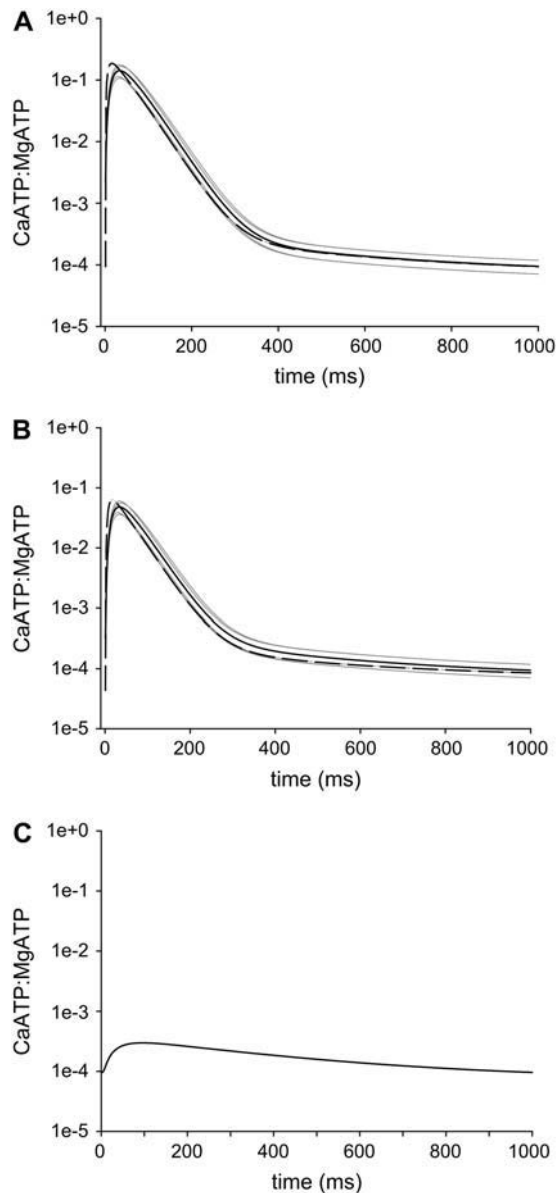
FIGURE 5 CaATP/MgATP generated within the model. (*A* and *B*) Ratios within the dyad; broken line represents raw CaATP/MgATP ratio, bold black line represents the PKA-CaATP/PKA-MgATP-bound occupancy ratio using the same kinetics for both CaATP and MgATP binding to PKA. The gray lines show the effect of varying CaATP-binding kinetics by $\pm25\%$. (*A*) The ratio at $r = 1$, (*B*) across the dyad as a whole, and (*C*) average ratio throughout the cytosol.

mouth) for the duration of the transient (28% across the whole dyad). As the rate of diffusion within the dyad is essentially an informed estimate based upon the diffusion in the free cytosol (5), we varied the dyadic diffusion coefficient to understand the impact an error in the original estimate may have. Peskoff and Langer (5) assume that due to the physical constants of diffusion (as described in the introduction) within the dyad, the rate of diffusion will be a third of that of the cytosol. Fig. 6, *D* and *E*, shows the

reduction in PKA activity predicted by our model if no such reduction in diffusion is assumed within the dyad. Fig. 6 *D* shows the effect at the channel mouth, with Fig. 6 *E* illustrating the reduction in PKA activity throughout the dyad. As could be expected an increase in the diffusion rate blunts the magnitude of the reduction in PKA activity at both locations, leading to peak reductions of 38% and 19% in PKA activity located near to the channel mouth and throughout the dyad, respectively. We also modeled the effect of underestimating the restriction of diffusion within the dyad by halving the rates proposed by Peskoff and Langer (5) (Fig. 6, *F* and *G*). Under these conditions the reduction in PKA activity is magnified, resulting in peak inhibitions of 65% and 50% for PKA near the channel mouth and throughout the dyad, respectively.

DISCUSSION

In this study, we sought to examine if the high $[Ca^{2+}]$ in the cardiac muscle dyadic space would influence the enzymatic activity of a protein kinase that phosphorylates protein targets resident in these spaces. PKA was shown to be inhibited at high $[Ca^{2+}]$ in a manner consistent with competitive inhibition of MgATP binding by CaATP. The physiological significance of these observations was explored using a mathematical model of a ventricular myocyte (half) sarcomere. The model was generated using structurally accurate subcellular compartments (dyadic volume) and kinetic parameters (fluxes, buffering, diffusion). The model produced physiological realistic cytosolic Ca^{2+} transients. $[Ca^{2+}]_{dyad}$ rose to concentrations exceeding 2 mM at sites close to the channel mouth and peaked at 300 μM across the dyadic cleft. This elevated $[Ca^{2+}]_{dyad}$ caused a pronounced shift in the CaATP/MgATP ratio, which in turn was predicted to inhibit PKA activity by 55% at the mouth of the channel and 40% across the cleft. The extent of inhibition varied temporally and was significant for the first 200 ms of a Ca^{2+} transient, with the average level of inhibition throughout the transient being 8% (calculated at a Ca^{2+} transient frequency of 1 Hz). PKA activity in the cytosol was unaffected by the modest elevation in CaATP/MgATP in that space, even regions close to the cleft, such as the corbular SR would be unlikely to experience inhibition of kinase activity, although it must be noted we do not include Ca^{2+} release from the corbular SR itself, which could alter this conclusion.

Our experimental data show that increasing $[Ca^{2+}]$ does inhibit PKA by increasing the level of CaATP, as there is a direct relationship between the activity of PKA and the CaATP/MgATP ratio, independent of total $[Ca^{2+}]$ or $[Mg^{2+}]$. CaATP is likely acting as a competitive inhibitor of MgATP binding to PKA.

We developed a computer simulation to predict the changes in the $[Ca^{2+}]$ and CaATP/MgATP ratio during a Ca^{2+} transient, generated in a ventricular myocyte. The model was based upon Bazzazi et al. (27), with Ca^{2+} buffering as
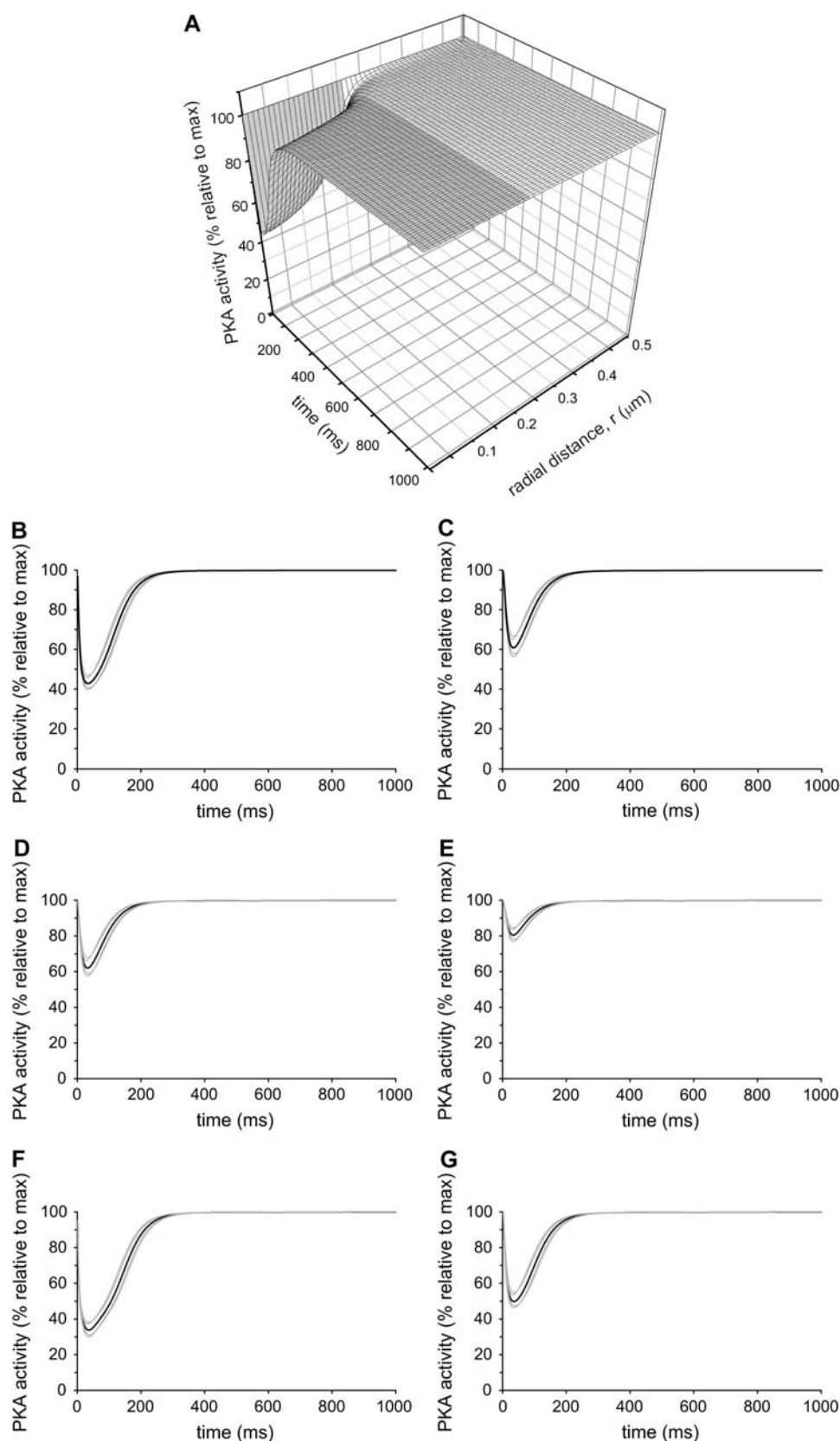
FIGURE 6 Transient inhibition of PKA activity in the dyad. (*A*) Three-dimensional plot of PKA activity at the Z-line ($z = 1$) as a function of time. The shaded region represents the dyadic space. (*B*) PKA activity at $r = 1$, akin to the 10-nm space immediately surrounding the RYR and DHPR channels and (*C*) averaged across the whole of the dyad. (*D* and *E*) As *B* and *C*, respectively, with double the dyadic diffusion rate. (*F* and *G*) As *B* and *C*, respectively, with half the dyadic diffusion rate. Black line represents equal CaATP and MgATP kinetics; gray lines show the effect of varying CaATP-binding kinetics by $\pm$ 25%.

described by Bers (10), with the addition of diffusible ATP and ADP able to bind Ca^{2+} or Mg^{2+} (30) and kinetic binding of CaATP and MgATP to PKA (24,31). Our model was able to simulate Ca^{2+} transients that replicated experimentally derived transients (8), in terms of both concentration and duration. In the simulation, $[Ca^{2+}]_{dyad}$ rose to over 2 mM at the Ca^{2+} release site and 300 μM averaged across the whole cleft. These $[Ca^{2+}]_{dyad}$ are within the range predicted by some, but not all, models of cardiac muscle (5,7–9). The discrepancy in predicted $[Ca^{2+}]_{dyad}$ may relate to the representation of Ca^{2+} influx as a ''common pool'' or ''all-or-none'' phenomenon in some models (5,7,8) (ours included) as opposed to a representation of entry as multiple stochastic events leading to more graded entries (9). We and others (5) used fixed Ca^{2+} entry derived experimentally, whereas other groups have used a change in membrane potential to estimate Ca^{2+} influx (7,8). Our $[Ca^{2+}]_{dyad}$ is also higher than that determined empirically using Na^{2+}/Ca^{2+} exchanger (NCX) currents to estimate near

membrane $[Ca^{2+}]$ (32). The data presented in Fig. 4 suggest that a steep $[Ca^{2+}]$ gradient occurs at the edge of the dyad; this coupled with the more recent data that NCXs are not localized within the dyad (33) suggest that NCXs would underestimate $[Ca^{2+}]_{dyad}$. The effects of reducing the peak $[Ca^{2+}]_{dyad}$ levels to those proposed by Michailova and McCulloch (30 μM) (7) are shown in Fig. 7, A and B. The 10-fold reduction in proposed $[Ca^{2+}]_{dyad}$ reduces the inhibition of PKA by 50%, (from 55% to 27%) at the Ca^{2+} release site and by 70% (from 40% to 12%) throughout the dyad as a whole. Although the effect on PKA activity is reduced under these conditions of lower $[Ca^{2+}]_{dyad}$, a 27% reduction in PKA activity could still prove significant. Fig. 7, C–F, shows the effect of varying the diffusion rates within the dyad, at 30 μM $[Ca^{2+}]_{dyad}$, as previously discussed for 300 μM in the results.

Our model shows that the high $[Ca^{2+}]_{dyad}$ causes a substantial shift in the CaATP/MgATP ratio within the dyadic cleft during a Ca^{2+} transient. At diastole CaATP/MgATP is
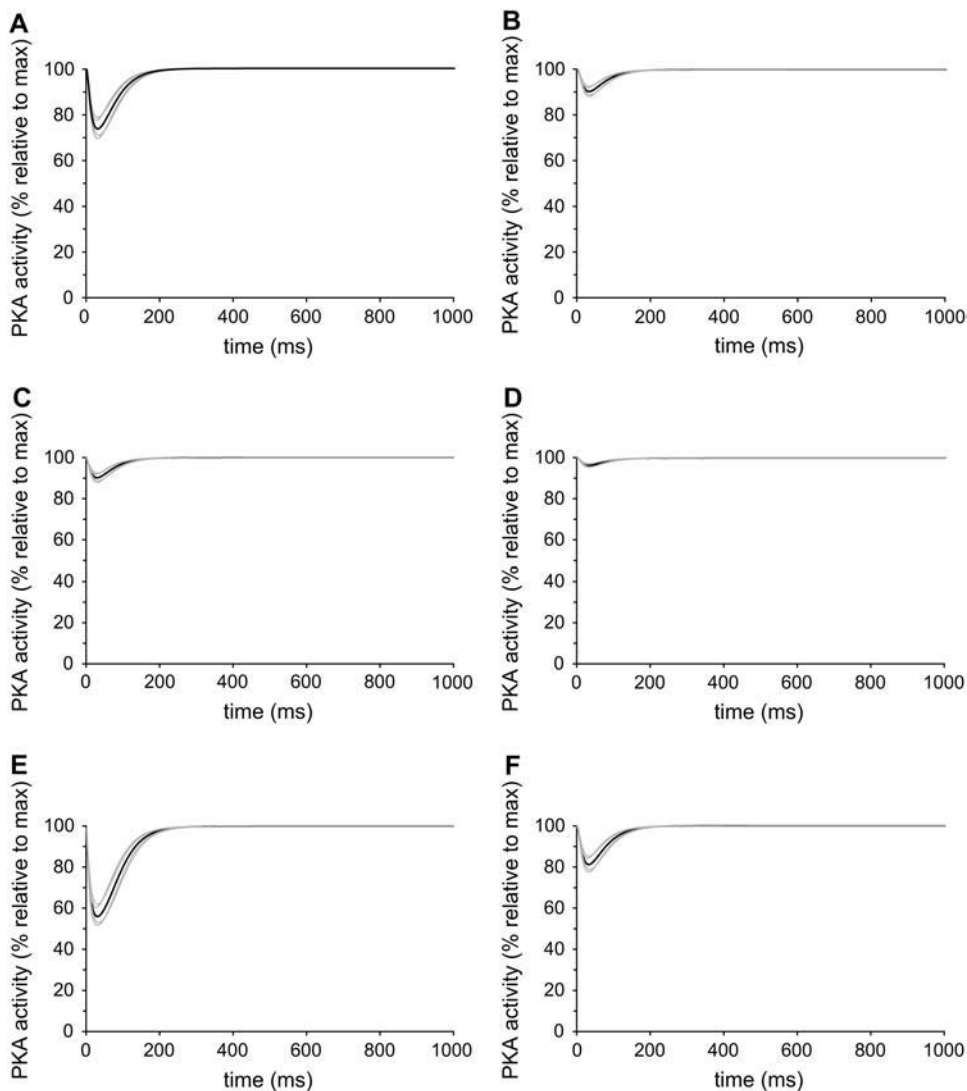

FIGURE 7 Transient inhibition of PKA activity in the dyad with reduced $[Ca^{2+}]_{dyad}$. PKA activity (A) at $r = 1$, akin to the 10-nm space immediately surrounding the RYR and DHPR channels and (B) averaged across the whole of the dyad, where $[Ca^{2+}]_{dyad}$ peaks a 30 μM. (C and D) As A and B, respectively, with double the dyadic diffusion rate. (E and F) As A and B, respectively, with half the dyadic diffusion rate. Black line represents equal CaATP and MgATP kinetics; gray lines show the effect of varying CaATP-binding kinetics by ± 25%.

9.4×10^{-5}, which quickly rises to 0.18 during systole. The ratio at systole is comparable with those predicted previously (34) in smooth muscle and in agreement with those predicted in cardiac muscle (7). The rate at which the CaATP/MgATP ratio alters over the initial 200 ms is faster than can be accommodated by kinetic binding of CaATP or MgATP to PKA. This leads to a delay between maximum of the CaATP/MgATP ratio and the PKA-CaATP/PKA-MgATP-bound ratio as is illustrated in Fig. 5, with the peak PKA-CaATP/PKA-MgATP bound ratio being 0.14.

Combining the experimental data describing the relationship of PKA activity and the CaATP/MgATP ratio with the simulated data predicting the bound PKA-CaATP/PKA-MgATP ratio transient within the dyadic cleft allowed us to predict the extent to which PKA activity would be reduced. The reduction in PKA activity peaked at ~55% and was maintained ~40% for 100 ms at a stimulatory frequency of 1 Hz.

To understand the full implication of a 40%–55% transient reduction in PKA activity on the phosphorylation status of dyadic proteins, it is necessary to have estimates of the level of activity (relative to theoretical maximum in vitro) required to maintain or increase the phosphorylation of the various proteins and channels residing in the dyadic cleft; however the empirical information regarding this region is not currently available. Our model does not attempt to predict the effect increasing CaATP may have on other dyadic enzymes, such as the phosphatases opposing PKA activity. Phosphatase activity is unlikely to be modulated by an increase in CaATP, as ATP is not a substrate, but the high $[Ca^{2+}]_{dyad}$ alone could affect Ca^{2+}-dependent phosphatases, although the effect on PKA described would be in addition to any other factors modulating dyad phosphorylation status. Recent models (17) have proposed that PKA is targeted to the dyad through muscle A kinase anchoring protein (mAKAP) as part of the RYR macromolecular complex. If this is the case it would lead to a high ratio of enzyme/substrate. This may counter some of the effect of CaATP on PKA and reflect a requirement for robust phosphorylation level of local proteins, although in this PKA-targeted model, PKA would be localized near the channel mouth and therefore experience the greatest level of inhibition predicted by our simulation.

There are perhaps greater implications for the effect of CaATP at higher stimulation frequencies. As there are no major Ca^{2+} removal mechanisms described as being located within the dyadic cleft, the major factors influencing $[Ca^{2+}]_{dyad}$ are Ca^{2+} entry and the diffusion rate through and out of the dyad. This would suggest that at higher stimulation frequencies (i.e., during exercise or those found in small mammals), where diffusion rates and Ca^{2+} entry would remain the same, $[Ca^{2+}]_{dyad}$ would remain at elevated levels for much more of the transient. At a contraction frequency of ~3 Hz (human during exercise) our current model would suggest $[Ca^{2+}]_{dyad}$ remains ~10 μM for half of the contraction cycle, this would equate to a 14%–24% reduction in activity even at diastole. In small mammals Peskoff et al. (6)

have suggested that at a frequency of ~7 Hz (a typical heart rate of rats), the $[Ca^{2+}]_{dyad}$ remains above 100 μM for half of the contraction cycle. This would lead to a chronic reduction in PKA activity (~30% reduction during diastole), agreeing well with the integration of our data, suggesting an average reduction in PKA activity throughout a Ca^{2+} transient at 7 Hz stimulation frequency of 28%. It would be interesting to examine what strategies are employed in these situations to achieve rapid and efficient phosphorylation of target proteins in an environment unfavorable to protein kinase action.

REFERENCES

1. Bers, D. M. 2002. Cardiac excitation-contraction coupling. *Nature.* 415:198–205.

2. Berne, R. M., and M. N. Levy. 1993. Physiology. Mosby Year Book, St. Louis, MO.

3. Shannon, T. R., and D. M. Bers. 2004. Integrated Ca2+ management in cardiac myocytes. *Ann. N. Y. Acad. Sci.* 1015:28–38.

4. Fabiato, A. 1983. Calcium-induced release of calcium from the cardiac sarcoplasmic reticulum. *Am. J. Physiol.* 245:C1–14.

5. Peskoff, A., and G. A. Langer. 1998. Calcium concentration and movement in the ventricular cardiac cell during an excitation-contraction cycle. *Biophys. J.* 74:153–174.

6. Peskoff, A., J. A. Post, and G. A. Langer. 1992. Sarcolemmal calcium binding sites in heart: II. Mathematical model for diffusion of calcium released from the sarcoplasmic reticulum into the diadic region. *J. Membr. Biol.* 129:59–69.

7. Michailova, A., and A. McCulloch. 2001. Model study of ATP and ADP buffering, transport of Ca(2+) and Mg(2+), and regulation of ion pumps in ventricular myocyte. *Biophys. J.* 81:614–629.

8. Winslow, R. L., J. Rice, S. Jafri, E. Marban, and B. O'Rourke. 1999. Mechanisms of altered excitation-contraction coupling in canine tachycardia-induced heart failure, II: model studies. *Circ. Res.* 84: 571–586.

9. Rice, J. J., M. S. Jafri, and R. L. Winslow. 1999. Modeling gain and gradedness of Ca2+ release in the functional unit of the cardiac diadic space. *Biophys. J.* 77:1871–1884.

10. Bers, D. M. 2001. Excitation-Contraction Coupling and Cardiac Contractile Force. Kluwer Academic Publishers, Dordrecht, The Netherlands.

11. Reuter, H. 1967. The dependence of slow inward current in Purkinje fibres on the extracellular calcium-concentration. *J. Physiol.* 192:479–492.

12. Rousseau, E., and G. Meissner. 1989. Single cardiac sarcoplasmic reticulum Ca2+-release channel: activation by caffeine. *Am. J. Physiol.* 256:H328–H333.

13. Xu, L., A. Tripathy, D. A. Pasek, and G. Meissner. 1998. Potential for pharmacology of ryanodine receptor/calcium release channels. *Ann. N. Y. Acad. Sci.* 853:130–148.

14. Rodriguez, P., M. S. Bhogal, and J. Colyer. 2003. Stoichiometric phosphorylation of cardiac ryanodine receptor on serine 2809 by calmodulin-dependent kinase II and protein kinase A. *J. Biol. Chem.* 278:38593–38600.

15. Witcher, D. R., R. J. Kovacs, H. Schulman, D. C. Cefali, and L. R. Jones. 1991. Unique phosphorylation site on the cardiac ryanodine receptor regulates calcium channel activity. *J. Biol. Chem.* 266:11144–11152.

16. Witcher, D. R., B. A. Strifler, and L. R. Jones. 1992. Cardiac-specific phosphorylation site for multifunctional Ca2+/calmodulin-dependent protein kinase is conserved in the brain ryanodine receptor. *J. Biol. Chem.* 267:4963–4967.

17. Marx, S. O., S. Reiken, Y. Hisamatsu, T. Jayaraman, D. Burkhoff, N. Rosemblit, and A. R. Marks. 2000. PKA phosphorylation dissociates FKBP12.6 from the calcium release channel (ryanodine receptor): defective regulation in failing hearts. *Cell.* 101:365–376.

18. Hain, J., H. Onoue, M. Mayrleitner, S. Fleischer, and H. Schindler. 1995. Phosphorylation modulates the function of the calcium release channel of sarcoplasmic reticulum from cardiac muscle. *J. Biol. Chem.* 270:2074–2081.

19. Valdivia, H. H., J. H. Kaplan, G. C. Ellis-Davies, and W. J. Lederer. 1995. Rapid adaptation of cardiac ryanodine receptors: modulation by Mg2+ and phosphorylation. *Science.* 267:1997–2000.

20. Reiken, S., M. Gaburjakova, S. Guatimosim, A. M. Gomez, J. D'Armiento, D. Burkhoff, J. Wang, G. Vassort, W. J. Lederer, and A. R. Marks. 2003. Protein kinase A phosphorylation of the cardiac calcium release channel (ryanodine receptor) in normal and failing hearts. Role of phosphatases and response to isoproterenol. *J. Biol. Chem.* 278:444–453.

21. Xiao, B., M. T. Jiang, M. Zhao, D. Yang, C. Sutherland, F. A. Lai, M. P. Walsh, D. C. Warltier, H. Cheng, and S. R. Chen. 2005. Characterization of a novel PKA phosphorylation site, serine-2030, reveals no PKA hyperphosphorylation of the cardiac ryanodine receptor in canine heart failure. *Circ. Res.* 96:847–855.

22. Maxwell, R. A., W. H. Welch, and D. A. Schooley. 2002. Juvenile hormone diol kinase. I. Purification, characterization, and substrate specificity of juvenile hormone-selective diol kinase from Manduca sexta. *J. Biol. Chem.* 277:21874–21881.

23. Mendlein, J., and G. Sachs. 1989. The substitution of calcium for magnesium in H+,K+-ATPase catalytic cycle. Evidence for two actions of divalent cations. *J. Biol. Chem.* 264:18512–18519.

24. Bhatnagar, D., R. Roskoski Jr., M. S. Rosendahl, and N. J. Leonard. 1983. Adenosine cyclic 3′,5′-monophosphate dependent protein kinase: a new fluorescence displacement titration technique for characterizing the nucleotide binding site on the catalytic subunit. *Biochemistry.* 22:6310–6317.

25. Brooks, S. P., and K. B. Storey. 1992. Bound and determined: a computer program for making buffers of defined ion concentrations. *Anal. Biochem.* 201:119–126.

26. Hinch, R., J. L. Greenstein, A. J. Tanskanen, L. Xu, and R. L. Winslow. 2004. A simplified local control model of calcium-induced calcium release in cardiac ventricular myocytes. *Biophys. J.* 87:3723–3736.

27. Bazzazi, H., M. E. Kargacin, and G. J. Kargacin. 2003. Ca2+ regulation in the near-membrane microenvironment in smooth muscle cells. *Biophys. J.* 85:1754–1765.

28. Yuan, W., K. S. Ginsburg, and D. M. Bers. 1996. Comparison of sarcolemmal calcium channel current in rabbit and rat ventricular myocytes. *J. Physiol.* 493:733–746.

29. Cleemann, L., W. Wang, and M. Morad. 1998. Two-dimensional confocal images of organization, density, and gating of focal Ca2+ release sites in rat cardiac myocytes. *Proc. Natl. Acad. Sci. USA.* 95:10984–10989.

30. Baylor, S. M., and S. Hollingworth. 1998. Model of sarcomeric Ca2+ movements, including ATP Ca2+ binding and diffusion, during activation of frog skeletal muscle. *J. Gen. Physiol.* 112:297–316.

31. Lew, J., S. S. Taylor, and J. A. Adams. 1997. Identification of a partially rate-determining step in the catalytic mechanism of cAMP-dependent protein kinase: a transient kinetic study using stopped-flow fluorescence spectroscopy. *Biochemistry.* 36:6717–6724.

32. Weber, C. R., V. Piacentino 3rd, K. S. Ginsburg, S. R. Houser, and D. M. Bers. 2002. Na(+)-Ca(2+) exchange current and submembrane [Ca(2+)] during the cardiac action potential. *Circ. Res.* 90:182–189.

33. Scriven, D. R., P. Dan, and E. D. Moore. 2000. Distribution of proteins implicated in excitation-contraction coupling in rat ventricular myocytes. *Biophys. J.* 79:2682–2691.

34. Kargacin, M. E., and G. J. Kargacin. 1997. Predicted changes in concentrations of free and bound ATP and ADP during intracellular Ca2+ signaling. *Am. J. Physiol.* 273:C1416–C1426.

35. Bernengo, J. C., C. Collet, and V. Jacquemond. 2001. Intracellular Mg2+ diffusion within isolated rat skeletal muscle fibers. *Biophys. Chem.* 89:35–51.

36. Gao, W. D., P. H. Backx, M. Azan-Backx, and E. Marban. 1994. Myofilament Ca2+ sensitivity in intact versus skinned rat ventricular muscle. *Circ. Res.* 74:408–415.

37. Robertson, S. P., J. D. Johnson, and J. D. Potter. 1981. The time-course of Ca2+ exchange with calmodulin, troponin, parvalbumin, and myosin in response to transient increases in Ca2+. *Biophys. J.* 34:559–569.

38. Pan, B. S., and R. J. Solaro. 1987. Calcium-binding properties of troponin C in detergent-skinned heart muscle fibers. *J. Biol. Chem.* 262:7839–7849.

39. Haiech, J., C. B. Klee, and J. G. Demaille. 1981. Effects of cations on affinity of calmodulin for calcium: ordered binding of calcium ions allows the specific activation of calmodulin-stimulated enzymes. *Biochemistry.* 20:3890–3897.

40. Post, J. A., and G. A. Langer. 1992. Sarcolemmal calcium binding sites in heart: I. Molecular origin in ''gas-dissected'' sarcolemma. *J. Membr. Biol.* 129:49–57.

41. Bers, D. M., L. V. Hryshko, S. M. Harrison, and D. D. Dawson. 1991. Citrate decreases contraction and Ca current in cardiac muscle independent of its buffering action. *Am. J. Physiol.* 260:C900–C909.

42. Blaustein, M. P., and W. J. Lederer. 1999. Sodium/calcium exchange: its physiological implications. *Physiol. Rev.* 79:763–854.